Strain Effect in Palladium Nanostructures as Nanozymes

Zheng Xi,[†,#] Xun Cheng,[‡,#] Zhuangqiang Gao,[†] Mengjing Wang,[∥] Tong Cai,[§] Michelle Muzzio,[§] Edwin Davidson,[∥] Ou Chen,[§] Yeonwoong Jung,[∥,⊥,Δ] Shouheng Sun,[§] Ye Xu,[‡,*] and Xiaohu Xia[†,∥,*]

[†]*Department of Chemistry,* [∥]*NanoScience Technology Center,* [⊥]*Department of Materials Science and Engineering*, *and* [Δ]*Department of Electrical and Computer Engineering*, *University of Central Florida, Orlando, Florida 32816, United States*

[‡]*Cain Department of Chemical Engineering, Louisiana State University, Baton Rouge, Louisiana 70803, United States*

[§]*Department of Chemistry, Brown University, Providence, Rhode Island 02912, United States*

[#]*These two authors contributed equally to this work.*

[*]*Corresponding author. E-mails: yexu@lsu.edu (Y.X.) and Xiaohu.Xia@ucf.edu (X.X.)*

Abstract

While various effects of physicochemical parameters (*e.g.*, size, facet, composition, and internal structure) on the catalytic efficiency of nanozymes (*i.e.*, nanoscale enzyme mimics) have been studied, the strain effect has never been reported and understood before. Herein, we demonstrate the strain effect in nanozymes by using Pd octahedra and icosahedra with peroxidase-like activities as a model system. Strained Pd icosahedra were found to display 2-fold higher peroxidase-like catalytic efficiency than unstrained Pd octahedra. Theoretical analysis suggests that tensile strain is more beneficial to OH radical (a key intermediate for the catalysis) generation than compressive strain. Pd icosahedra are more active than Pd octahedra because icosahedra amplify the surface strain field. As a proof-of-concept demonstration, the strained Pd icosahedra were applied to immunoassay of biomarkers, outperforming both unstrained Pd octahedra and natural peroxidases. The findings in this research may serve as a strong foundation to guide the design of high-performance nanozymes.

Table of Contents

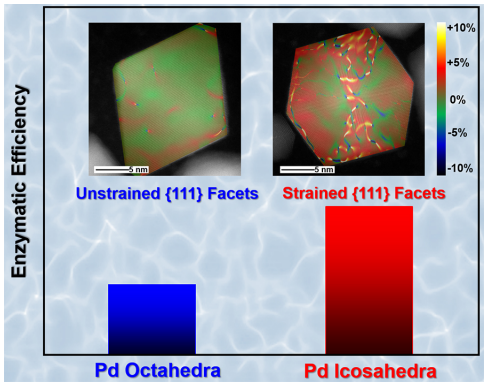

Keywords: Palladium nanostructures · strain effect · enzyme mimic · catalysis · immunoassay

Recent extensive studies on nanoscale enzyme mimics (typically known as "nanozymes") have drawn great attention due to their promising potentials in various applications, such as biosensing,[1,2] imaging,[3,4] therapy,[5,6] and environmental protection.[7] Compared to natural enzymes as counterparts, nanozymes are usually much more stable because they are less vulnerable to changes in the catalytic environment (*e.g.*, pH and temperature).[8] With superior stability, significant efforts in developing nanozymes have been devoted to enhancing the catalytic efficiency that largely determines the performance of these nanozymes in certain applications.[9] Improvement of catalytic efficiency is rooted in a fundamental understanding of the structure-property relationship. To this end, effects of particle size,[10] facet exposure on the surface,[11,12] elemental composition,[13,14] surface capping ligands,[15] and internal structure (solid *versus* hollow)[16,17] on the catalytic efficiency of nanozymes have been broadly investigated.

In conventional heterogeneous catalysis, surface strain has been proven to be a critical parameter that affects the activity of a catalyst. Surface strain, which is generally caused by lattice mismatch between different components or the intrinsic twin structures, can modify the surface electronic structure through a change of surface atomic distances, thus altering the interaction between reaction intermediates and surfaces and in turn tuning catalytic activity.[18,19] For instance, previous work on platinum nanostructure demonstrated the catalytic surface with only 1% compressive lattice strain could appreciably alter the adsorption energies of key reaction intermediates.[20] Engineering the surface strain as an effective strategy to enhance catalytic activity has been extensively used in many industrially important reactions such as oxygen reduction,[18,19,21] formic acid oxidation,[22] and CO_2 reduction[23]. Nevertheless, to the best of our knowledge, strain effect has never been reported in nanozyme development so far.

In this work, we design an ideal platform based on Pd octahedra and icosahedra with peroxidase-like activities to investigate the strain effect on the catalytic efficiency of nanozymes. We chose peroxidase as a model enzymatic system for demonstration because artificial peroxidases have been actively developed and widely used in recent years, and their catalytic efficiency can be conveniently quantified with a simple spectrophotometer.[2,13] Our experimental results showed that strained Pd icosahedra display much higher peroxidase-like catalytic efficiencies than unstrained Pd octahedra. Theoretical analysis based on density functional theory (DFT) calculations, which takes surface strain and surface coverage into consideration, suggests that tensile strain is more beneficial to the generation of OH radical as a key intermediate for the catalysis than compressive strain. The amplification of the surface strain field as seen on the Pd icosahedra imparts both more stretched and more compressed surface areas, which results in a noticeable increase in peroxidase-like efficiency overall. As a proof-of-concept demonstration, we applied the Pd icosahedra to colorimetric detection of carcinoembryonic antigen (CEA, a common cancer biomarker)[24], which provided a higher detection sensitivity compared to both Pd

octahedra- and natural peroxidase-based assays.

To construct such a platform, Pd octahedra and icosahedra with the same type of facet on the surface and similar sizes were prepared according to previous reports (see Supporting Information (SI) and Figure S1 for details).[25,26] The representative transmission electron microscopy (TEM, Figure 1A and 1B) images of the Pd octahedra and icosahedra suggest both nanostructures were obtained in high purity and good uniformity. The average sizes of Pd octahedra and icosahedra were measured to be 19.2 ± 1.8 and 19.5 ± 1.3 nm, respectively, by randomly analyzing more than 400 particles of each nanostructure (Figure S2). To reveal detailed structures, atomic resolution high-angle annular dark-field scanning TEM (HAADF-STEM) images of an individual Pd octahedron (Figure 1C) and icosahedron (Figure 1D) were obtained. The twin boundaries on icosahedron could be clearly seen in Figure 1D. The *d* (111) spacing for the octahedron was measured to be 2.23 Å, close to the single-crystalline bulk (2.25 Å).[23] In contrast, the *d* (111) spacing for the icosahedron varies with different regions. The interatomic distances near the twin boundaries were measured to be 2.17 Å, indicating a ~2.5% compressive strain than octahedron, while those at the central faces were 2.33 Å, indicating a ~4.5% tensile strain. These different strains are caused by the unique intrinsic structure of the icosahedral shape and the strong distortions near twin boundaries.[27,28] The X-ray diffraction (XRD) patterns (Figure 1E) showed that all the major peaks of icosahedra were shifted to lower angles with respect to those of octahedra, indicating the stretched lattice constant of icosahedra.[27] Meanwhile, the small hump at higher angle in (111) diffraction peak indicates the existence of highly compressed areas in icosahedra.[27] Notably, all peaks of icosahedra were broader than those of octahedra, suggesting the icosahedra are twin defect-rich.[29] These data clearly demonstrate the co-existence of tensile and compressive strains on icosahedral facets, as well as the negligible strain on octahedral facets, which are consistent with the electron microscopy analyses. The thermal gravimetric analysis (TGA) (Figure S3) showed both Pd octahedra and icosahedra had similar weight percentage of residual capping agent (polyvinylpyrrolidone (PVP)) on surface. The PVP packing density on Pd octahedra and icosahedra were estimated to be 9.2×10^{-3} and 8.5×10^{-3} nm^{-2} respectively according to the TGA weight loss and the Pd size and shape,[30,31] suggesting the similar surface ligand coverage density of both Pd nanostructures. Electrochemical copper-based underpotential deposition (Cu_{UPD}) was used to measure the surface areas of both Pd nanostructures.[32] Figure S4 shows the cyclic voltammetry (CV) curves of Cu UPD on Pd nanostructures, where the dominant pair peaks around 0.4 V on the curves can be ascribed to the Cu dissolution and deposition on Pd (111) surfaces.[33] Based on the Cu stripping curves, the accessible surface areas of Pd octahedra and icosahedra normalized to the

mass in solution phase were determined to be 33.33 m^2 g^{-1} and 38.46 m^2 g^{-1}, respectively, assuming monolayer Cu deposition on Pd surfaces and charge density 480 μC cm^{-2}.[32] Notably, the surface areas measured by Cu UPD are very close to the calculated geometric surface areas (*i.e.*, 32.21 m^2 g^{-1} for Pd octahedra and 32.22 m^2 g^{-1} for Pd icosahedra).[32] Collectively, these two types of Pd nanostructures, which have the same type of (111) facet exposure and capping agent on surface, similar sizes, ligand coverage densities and surface areas, but different surface strains, could serve as an ideal platform to investigate the strain effect in nanozyme catalysis.

We then evaluated the peroxidase-like activities of the two Pd nanostructures. Oxidation of 3,3',5,5' - tetramethylbenzidine (TMB, a typical peroxidase substrate[34]) by H_2O_2, which yields a blue-colored product with λ_{max} = 653 nm (*i.e.*, oxidized TMB[34]), was employed as a model catalytic reaction. As shown by Figure 2A, Pd icosahedra were more active in catalyzing the reaction relative to Pd octahedra, generating a more intense blue-colored reaction solution. To quantify their catalytic efficiencies, apparent steady-state kinetic assay was performed (see the SI for details). Typical Michealis-Menten curves were obtained for both Pd nanostructures by plotting initial reaction velocities against TMB concentrations (Figure 2B). These curves were then fitted to the double-reciprocal plots (Figure 2C), from which the kinetic parameters of both Pd nanostructures were derived (Table S1).[35] The catalytic efficiency of Pd icosahedra in terms of K_{cat} (defined as the maximum number of substrate conversions per second per catalyst) was much higher than those of Pd octahedra and horseradish peroxidase (HRP, a typical natural peroxidase).[2] For direct comparison, we derived the specific catalytic efficiencies ($K_{cat\text{-}specific}$) of the Pd nanostructures by normalizing K_{cat} to the surface area measured from Cu_{UPD} of an individual catalyst. As summarized in Figure 2D, the $K_{cat\text{-}specific}$ value of Pd icosahedra was 3.0×10^{2} $s^{-1}nm^{-2}$, 2-fold higher than the value of Pd octahedra.

To understand the correlation between the improved peroxidase-like catalytic efficiency and the strained Pd icosahedron surface, we investigated on the mechanism of H_2O_2 decomposition by density functional theory (DFT)-based approaches. Previous theoretical studies postulated that on a clean Pd surface H_2O_2 can be readily broken down into atomic O following $H_2O_2 \rightarrow 2OH^* \rightarrow H_2O + O^*$ (* denotes a surface-adsorbate species), with O* being the oxidant to TMB.[11,36,37] However, the desorption of O* or OH* from Pd surface into solution toward oxidizing TMB is hindered by the strong adsorption energies[38] (Table S2). Moreover, with some amount of O* built up on the surface, the reactivity of H_2O_2 quickly switches to a dehydrogenation pathway following $H_2O_2 \rightarrow OOH^* \rightarrow O_2^* \rightarrow O_2\uparrow$.[38] Thus, the most likely oxidant is OH radicals formed directly in solution. In order to confirm this, we performed electron paramagnetic resonance (EPR) analysis to detect OH radical in solution, where 5,5-dimethyl-1-pyrroline N-oxide

(DMPO) was used to capture OH radicals.[39] As shown by Figure S5, characteristic 1:2:2:1 EPR peaks for DMPO-OH adduct can be clearly observed, suggesting the existence of OH radicals in solution.[39] To further demonstrate the formation of OH radicals in catalytic reaction solution, we performed an additional control experiment. Specifically, a scavenger for OH radical in solution – *tert*-butanol (TBA, see Figure S6A)[40] – was added to the catalytic reaction (*i.e.*, oxidation of TMB by H_2O_2). As shown by Figure S6B, TBA actively consumed the OH radicals formed in solution and thus dramatically decreased the catalytic activity as indicated by the UV absorbance at 653 nm. This control experiment, along with the EPR analysis, clearly demonstrated the formation of OH radicals in solution. We therefore propose that OH radicals in solution must be generated from an alternate, reverse Eley-Rideal-type step, the reactant being either OOH* or H_2O_2.[38] We surmise this process (*e.g.*, for OOH*) to involve the shuttling of a neutral H atom through bulk water to OOH* driven by thermal fluctuations, forming an OOHH* intermediate that immediately decomposes to H_2O and an adsorbed O*, effectively forming an OH radical in solution. As such, the stability of O* directly affects the kinetics of this step, and it is in turn affected by both surface strain and coverages of intermediates (*e.g.*, O*).

To ascertain the strain effect, we developed a microkinetic model based on a simplified H_2O_2 decomposition mechanism on Pd (111) after Plauck et al.[38] (see mechanism in Table S3), using self-consistent GGA-RPBE energetics. It contained the key steps for O-O bond scission, H transfer, and H_2O and O_2 formation with four surface species: O*, OH*, OOH*, and H_2O* (Figure S7). The OH radical formation steps outlined above were treated as a perturbation on this mechanism. The outcome of our analysis is plotted in Figure 3A. Most noticeably, the model predicts that the rate of OH radical formation increases with tensile strain on Pd (111). This is due to increasing coverage of OOH* and O* with tensile strain and due to the counteracting effects of strain and coverage on the activation energy (Figure S8).

We then propose that the uniqueness of Pd icosahedra catalytic activity stems from the amplification of surface strain fields in both tensile and compressive directions, which can be verified by surface strain mapping using geometric phase analysis (GPA).[41,42] Based on GPA results (Figure 3B), the icosahedra exhibit a wider range strain distribution relative to the octahedra. In a simple scenario, if we take ±1.0% and ±2.0% as representative strain values obtained from a linear strain scan for an octahedron and icosahedron respectively, as shown in Figure 3C, with half of the surface exhibiting the compressive strain and the other half exhibiting the opposite tensile strain, we arrive at the conclusion, based on the microkinetic results in Figure 3A, that the icosahedron should be 2.5 times more active at generating OH radicals than the octahedron, considering the similar surface areas of two Pd nanoparticles. This agrees well

with our experimental measurements (2 times). It should also be mentioned that the coordination number (CN) of edge atoms on Pd octahedra and icosahedra are similar, which are 7 and 8, respectively.[23,28] As shown in Figure S9, the *d*-band center of a representative edge site (using Pd (221) facet with 0% strain as model), with the same CN (7) as edge atoms on Pd octahedra, would suggest its reactivity to be equivalent to that of a Pd (111) facet with ~ 3% tensile strain. An edge atom with CN=7 that is also under compressive strain, or an edge atom with CN=8 (same CN as edge atoms on Pd icosahedra) under tensile strain,[23] should have lower *d*-band centers than that of edge atoms on 0% strained Pd (221). This would place the catalytic activity of edge sites well within the spectrum of strain values that we have considered (Figure 3A). Moreover, edge atoms amount to small percentages of all surface atoms (4.6% for octahedra and 8.6% for icosahedra). Altogether, we do not expect them to significantly alter the activity ratio that we have estimated for octahedron *vs.* icosahedron (*i.e.*, 2.5).

Finally, to demonstrate potential use of the Pd icosahedra with enhanced enzymatic efficiency, we applied them as labels to colorimetric enzyme-linked immunosorbent assay (ELISA, a widely used technology for medical diagnostics[43]). Carcinoembryonic antigen (CEA, a common cancer biomarker[24]) was chosen as a model analyte. For comparison, Pd octahedra and HRP were also used as labels for the ELISA of CEA by using the same set of antibodies. Figure 4A illustrates the principle of the ELISA, which was established and performed according to our previously published procedures.[13] CEA standards of various concentrations were monitored in a 96-well microtiter plate (Figure 4B), where the yellow-colored product with λ_{max} = 450 nm (*i.e.*, diimine) was converted from oxidized TMB by quenching the catalytic reaction using H_2SO_4.[34] By quantifying the results shown in Figure 4B using a plate reader, calibration curves of the ELISAs were obtained (Figure 4C). For the Pd icosahedra-ELISA (red curves), quality linear relationship (r^2 = 0.997) in the range of 50-5,000 pg/mL was observed. The detection limit (defined by the 3SD method[44]) was determined to be 34 pg/mL. In comparison, the detection limits of Pd octahedra- and HRP-ELISAs were calculated to be 98 pg/mL and 434 pg/mL, respectively, based on their calibration curves (blue and black). This substantially increased detection sensitivity for the Pd icosahedra-ELISA could be mainly attributed to the much higher catalytic efficiency of the Pd icosahedra relative to Pd octahedra and HRP because all other conditions of the three ELISAs were kept identical.

In summary, we have demonstrated surface strain-dependent catalytic efficiency in nanozymes by using Pd octahedra and icosahedra with peroxidase-like activities as a model system. The strained Pd icosahedra show a 2-fold higher specific catalytic efficiency than unstrained Pd octahedra. The experimental findings were rationalized with DFT calculations

based on a reverse Eley-Rideal-type mechanism, which may be applicable to other metal mimics of peroxidase.[13] The strain enhanced catalytic efficiency of Pd icosahedra ensures their superior performance in immunoassay of biomarkers. This work not only demonstrates the strain effect but also provides an effective knob to tune the catalytic efficiency of nanozymes.

Supporting Information

The Supporting Information is available free of charge on the ACS Publications website.

Acknowledgments

This work was supported in part by grants from the National Science Foundation (CHE-1834874 and CBET-1804525), and the startup funds from University of Central Florida (UCF). Z.X. was partially supported by the UCF Preeminent Postdoctoral Program. X.C. and Y.X. acknowledge support by the U.S. Department of Energy, Office of Science, Basic Energy Sciences, Catalysis Science Program, under Award #DE-SC0018408 and high-performance computing resources provided by the Louisiana Optical Network Infrastructure and by the National Energy Research Scientific Computing Center, which is supported by the Office of Science of the U.S. Department of Energy under contract #DE-AC02-05CH11231. M. M. is supported by the National Science Foundation Graduate Research Fellowship, under Grant No. 1644760. The authors thank Dr. Xiaofeng Feng and Dr. Lin Hu of UCF for help with electrochemical analysis.

Competing Interests

The authors declare no competing interests.

References

1. Liu, B.; Sun, Z.; Huang, P.; Liu, J. Hydrogen Peroxide Displacing DNA from Nanoceria: Mechanism and Detection of Glucose in Serum. *J. Am. Chem. Soc.*, **2015**, *137*, 1290–1295.
2. Gao, L.; Zhuang, J.; Nie, L.; Zhang, J.; Zhang, Y.; Gu, N.; Wang, T.; Feng, J.; Yang, D.; Perrett, S.; Yan, X. Intrinsic Peroxidase-like Activity of Ferromagnetic Nanoparticles. *Nat. Nanotechnol.* **2007**, *2*, 577-583.
3. Fan, K.; Cao, C.; Pan, Y.; Lu, D.; Yang, D.; Feng, J.; Song, L.; Liang M.; Yan, X.

Magnetoferritin Nanoparticles for Targeting and Visualizing Tumour Tissues. *Nat. Nanotechnol.*, **2012**, *7*, 459–464.

4. Gupta, A.; Das, R.; Yesilbag Tonga, G.; Mizuhara, T.; Rotello,V. M. Charge-Switchable Nanozymes for Bioorthogonal Imaging of Biofilm-Associated Infections. *ACS Nano*, **2018**, *12*, 89–94.
5. Kim, C. K.; Kim, T.; Choi, I. Y.; Soh, M.; Kim, D.; Kim, Y. J.; Jang, H.; Yang, H. S.; Kim, J. Y.; Park, H. K.; Park, S. P.; Park, S.; Yu, T.; Yoon, B. W.; Lee, S. H.; Hyeon, T. Ceria Nanoparticles That Can Protect Against Ischemic Stroke. *Angew. Chem., Int. Ed.*, **2012**, *51*, 11039–11043.
6. Vernekar, A. A.; Sinha, D.; Srivastava, S.; Paramasivam, P. U.; D'Silva, P.; Mugesh, G. An Antioxidant Nanozyme that Uncovers the Cytoprotective Potential of Vanadia Nanowires. *Nat. Commun.*, **2014**, *5*, 5301.
7. Herget, K.; Hubach, P.; Pusch, S.; Deglmann, P.; Gotz, H.; Gorelik, T. E.; Gural'skiy, I. A.; Pfitzner, F.; Link, T.; Schenk, S.; Panthofer, M.; Ksenofontov, V.; Kolb, U.; Opatz, T.; Andre, R.; Tremel, W. Haloperoxidase Mimicry by CeO_{2-x} Nanorods Combats Biofouling. *Adv. Mater.*, **2017**, *29*, 1603823.
8. Wei, H.; Wang, E. Nanomaterials with Enzyme-like Characteristics (Nanozymes): Next-Generation Artificial Enzymes. *Chem. Soc. Rev.* **2013**, *42*, 6060-6093.
9. Wu, J.; Wang, X.; Wang, Q.; Lou, Z.; Li, S.; Zhu, Y.; Qin, L.; Wei, H. Nanomaterials with Enzyme-like Characteristics (Nanozymes): Next-Generation Artificial Anzymes (II). *Chem. Soc. Rev.* **2019**, *48*, 1004-1076.
10. Fu, Y.; Zhao, X.; Zhang, J.; Li, W. DNA-Based Platinum Nanozymes for Peroxidase Mimetics. *J. Phys. Chem. C* **2014**, *118*, 18116-18125.
11. Ge, C.; Fang, G.; Shen, X.; Chong, Y.; Wamer, W. G.; Gao, X.; Chai, Z.; Chen, C.; Yin, J. Facet Energy versus Enzyme-like Activities: The Unexpected Protection of Palladium Nanocrystals against Oxidative Damage. *ACS Nano* **2016**, *10*, 10436−10445.
12. Ghosh, S.; Roy, P.; Karmodak, N.; Jemmis, E. D.; Mugesh, G. Nanoisozymes: Crystal-Facet-Dependent Enzyme-Mimetic Activity of V_2O_5 Nanomaterials. *Angew. Chem., Int. Ed.* **2018**, *57*, 4510-4515.
13. Xia, X.; Zhang, J.; Lu, N.; Kim, M. J.; Ghale, K.; Xu, Y.; McKenzie, E.; Liu, J.; Ye, H. Pd-Ir Core-shell Nanocubes: A Type of Highly Efficient and Versatile Peroxidase Mimic. *ACS*

Nano **2015**, *9*, 9994−10004.

14. Gao, Z.; Ye, H.; Tang, D.; Tao, J.; Habibi, S.; Minerick, A.; Tang, D.; Xia, X. Platinum-decorated Gold Nanoparticles with Dual Functionalities for Ultrasensitive Colorimetric in Vitro Diagnostics. *Nano Lett.* **2017**, *17*, 5572−5579.
15. Wang, S.; Chen, W.; Liu, A.; Hong, L.; Deng, H.; Lin, X. Comparison of the Peroxidase-Like Activity of Unmodified, Amino-Modified, and Citrate-Capped Gold Nanoparticles. *ChemPhysChem* **2012**, *13*, 1199–1204.
16. Wu, R.; Chong, Y.; Fang, G.; Jiang, X.; Pan, Y.; Chen, C.; Yin, J.; Ge, C. Synthesis of Pt Hollow Nanodendrites with Enhanced Peroxidase-Like Activity against Bacterial Infections: Implication for Wound Healing. *Adv. Funct. Mater.* **2018**, *28*, 1801484.
17. Ge, S.; Liu, W.; Liu, H.; Liu, F.; Yu, J.; Yan, M.; Huang, J. Colorimetric Detection of the Flux of Hydrogen Peroxide Released from Living Cells Based on the High Peroxidase-like Catalytic Performance of Porous PtPd Nanorods. *Biosens. Bioelectron.* **2015**, *71*, 456-462.
18. Wang, H.; Xu, S.; Tsai, C.; Li, Y.; Liu, C.; Zhao, J.; Liu, Y.; Yuan, H.; Abild-Pedersen, F.; Prinz, F. B.; Norskov, J. K.; Cui, Y. Direct and Continuous Strain Control of Catalysts with Tunable Battery Electrode Materials. *Science* **2016**, *354*, 1031-1036.
19. Wang, L.; Zeng, Z.; Gao, W.; Maxson, T.; Raciti, D.; Giroux, M. Pan, X.; Wang, C.; Greeley, J. Tunable Intrinsic Strain in Two-Dimensional Transition Metal Electrocatalysts. *Science* **2019**, *363*, 870-874.
20. Strasser, P.; Koh, S.; Anniyev, T.; Greeley, J.; More, K.; Yu, C.; Liu, Z.; Kaya, S.; Nordlund, D.; Ogasawara, H.; Toney, M. F.; Nilsson, A. Lattice-Strain Control of the Activity in Dealloyed Core–Shell Fuel Cell Catalysts. *Nat. Chem.* **2010**, *2*, 454–460.
21. Li, M.; Zhao, Z.; Cheng, T.; Fortunelli, A.; Chen, C. Y.; Yu, R.; Zhang, Q.; Gu, L.; Merinov, B.; Lin, Z.; Zhu, E.; Yu, T.; Jia, Q.; Guo, J.; Zhang, L.; Goddard, W. A., 3rd; Huang, Y.; Duan, X. Ultrafine Jagged Platinum Nanowires Enable Ultrahigh Mass Activity for the Oxygen Reduction Reaction. *Science* **2016**, *354*, 1414-1419.
22. Xi, Z.; Erdosy, D. P.; Mendoza-Garcia, A.; Duchesne, P. N.; Li, J.; Muzzio, M.; Li, Q.; Zhang, P.; Sun, S. Pd Nanoparticles Coupled to $WO_{2.72}$ Nanorods for Enhanced Electrochemical Oxidation of Formic Acid. *Nano Lett.* **2017**, *17*, 2727-2731.
23. Huang, H.; Jia, H.; Liu, Z.; Gao, P.; Zhao, J.; Luo, Z.; Yang, J.; Zeng, J. Understanding of Strain Effects in the Electrochemical Reduction of CO_2: Using Pd Nanostructures as an Ideal

Platform. *Angew. Chem., Int. Ed.* **2017**, *56*, 3594-3598.

24. Benchimol, S.; Fuks, A.; Jothy, S.; Beauchemin, N.; Shirota, K.; Stanners, C. P. Carcinoembryonic Antigen, a Human-Tumor Marker, Functions as an Intercellular-Adhesion Molecule. *Cell* **1989**, *57*, 327-334.
25. Liu, M.; Zheng, Y.; Zhang, L.; Guo, L.; Xia, Y. Transformation of Pd Nanocubes into Octahedra with Controlled Sizes by Maneuvering the Rates of Etching and Regrowth. *J. Am. Chem. Soc.* **2013**, *135*, 11752-11755.
26. Huang, H.; Wang, Y.; Ruditskiy, A.; Peng, H.; Zhao, X.; Zhang, L.; Liu, J.; Ye, Z.; Xia, Y. Polyol Syntheses of Palladium Decahedra and Icosahedra as Pure Samples by Maneuvering the Reaction Kinetics with Additives. *ACS Nano* **2014**, *8*, 7041-7050.
27. Li, C.; Sato, R.; Kanehara, M.; Zeng, H.; Bando, Y.; Teranishi, T. Controllable Polyol Synthesis of Uniform Palladium Icosahedra: Effect of Twinned Structure on Deformation of Crystalline Lattices. *Angew. Chem., Int. Ed.* **2009**, *48*, 6883-6887.
28. Wu, J.; Qi, L.; You, H.; Gross, A.; Li, J.; Yang, H. Icosahedral Platinum Alloy Nanocrystals with Enhanced Electrocatalytic Activities. *J. Am. Chem. Soc.* **2012**, *134*, 11880-11883.
29. Kuo, C. H.; Lamontagne, L. K.; Brodsky, C. N.; Chou, L. Y.; Zhuang, J.; Sneed, B. T.; Sheehan, M. K.; Tsung, C. K. The Effect of Lattice Strain on the Catalytic Properties of Pd Nanocrystals. *ChemSusChem* **2013**, *6*, 1993-2000.
30. Ye, H.; Liu, Y.; Chhabra, A.; Lilla, E.; Xia, X. Polyvinylpyrrolidone (PVP)-Capped Pt Nanocubes with Superior Peroxidase-like Activity. *ChemNanoMat* **2017**, *3*, 33-38.
31. Wang, Y.; Biby, A.; Xi, Z.; Liu, B.; Rao, Q.; Xia, X. One-Pot Synthesis of Single-Crystal Palladium Nanoparticles with Controllable Sizes for Applications in Catalysis and Biomedicine. *ACS Appl. Nano Mater.* **2019**, *2*, 4605-4612.
32. Shao, M.; Odell, J. H.; Choi, S. II, Xia, Y. Electrochemical Surface Area Measurements of Platinum- and Palladium-based Nanoparticles. *Electrochem. Commun.* **2013**, *31*, 46-48.
33. Zhang, F.; Sheng, T.; Tian, N.; Li, L.; Xiao, C.; Lu, B.; Xu, B.; Zhou, Z.; Sun, S. Cu Overlayers on Tetrahexahedral Pd Nanocrystals with High-index Facets for CO_2 Electroreduction to Alcohols. *Chem. Commun.* **2017**, *53*, 8085-8088.
34. Josephy, P. D.; Eling, T. E.; Mason, R. P. The Horseradish Peroxidase-Catalyzed Oxidation of 3,5,3',5'-Tetramethylbenzidine. Free Radical and Charge-Transfer Complex Intermediates. *J. Biol. Chem.* **1982**, *257*, 3669-3675.

35. Lineweaver, H.; Burk, D. The Determination of Enzyme Dissociation Constants. *J. Am. Chem. Soc.* **1934**, *56*, 658-666.
36. Li, J.; Liu, W.; Wu, X.; Gao, X. Mechanism of pH-Switchable Peroxidase and Catalase-like Activities of Gold, Silver, Platinum and Palladium. *Biomaterials* **2015**, *48*, 37-44.
37. Wang, X.; Gao, X.; Qin, L.; Wang, C.; Song, L.; Zhou, Y.; Zhu, G.; Cao, W.; Lin, S.; Zhou, L.; Wang, K.; Zhang, H.; Jin, Z.; Wang, P.; Gao, X.; Wei, H. e_g Occupancy as an Effective Descriptor for the Catalytic Activity of Perovskite Oxide-based Peroxidase Mimics. *Nat. Commun.*, **2019**, *10*, 704.
38. Plauck, A.; Stangland, E. E.; Dumesic, J. A.; Mavrikakis, M. Active Sites and Mechanisms for H_2O_2 Decomposition over Pd Catalysts. *P. Natl. Acad. Sci. USA* **2016**, *113*, 1973-1982.
39. Khachatryan, L.; McFerrin, C. A.; Hall, R. W.; Dellinger, B. Environmentally Persistent Free Radicals (EPFRs). 3. Free versus Bound Hydroxyl Radicals in EPFR Aqueous Solutions. *Environ. Sci. Technol.* **2014**, *48*, 9220-9226.
40. Tauber, A.; Mark, G.; Schuchmann, H.; Sonntag, C. V. Sonolysis of *tert*-butyl Alcohol in Aqueous Solution. *J. Chem. Soc., Perkin Trans.* **1999**, *2*, 1129-1135.
41. Kim, K. H.; DigitalMicrograph Script Source Listing for a Geometric Phase Analysis. *Appl. Microsc.* **2015**, *45*, 101-105.
42. Hÿtch, M. J.; Snoeck, E.; Kilaas, R. Quantitative Measurement of Displacement and Strain Fields from HREM Micrographs. *Ultramicroscopy* **1998**, *74*, 131-146.
43. Lequin, R. M. Enzyme Immunoassay (EIA)/Enzyme-Linked Immunosorbent Assay (ELISA). *Clin. Chem.* **2005**, *51*, 2415-2418.
44. Armbruster, D. A.; Tillman, M. D.; Hubbs, L. M. Limit of Detection (LQD)/Limit of Quantitation (LOQ): Comparison of the Empirical and the Statistical Methods Exemplified with GC-MS Assays of Abused Drugs. *Clin. Chem.* **1994**, *40*, 1233–1238.

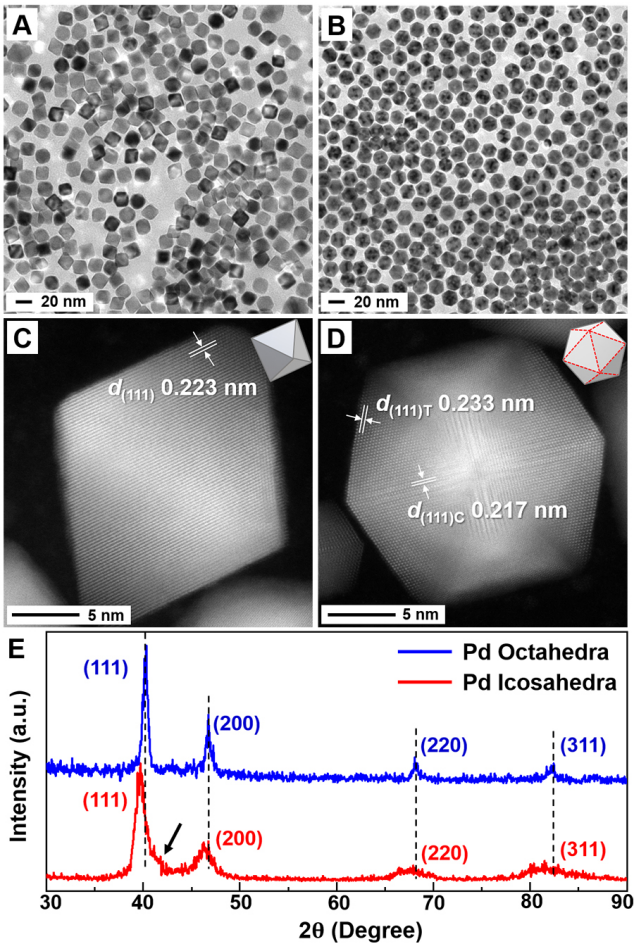

Figure 1. (A, B) TEM images of (A) Pd octahedra and (B) Pd icosahedra; (C, D) Atomic resolution HAADF-STEM images of individual (A) Pd octahedron and (B) Pd icosahedron. Insets show corresponding models of the nanostructures. Dashed red lines highlight twin planes; (E) XRD patterns recorded from Pd octahedra and icosahedra. The black arrow indicates the hump at higher angle of (111) diffraction peak.

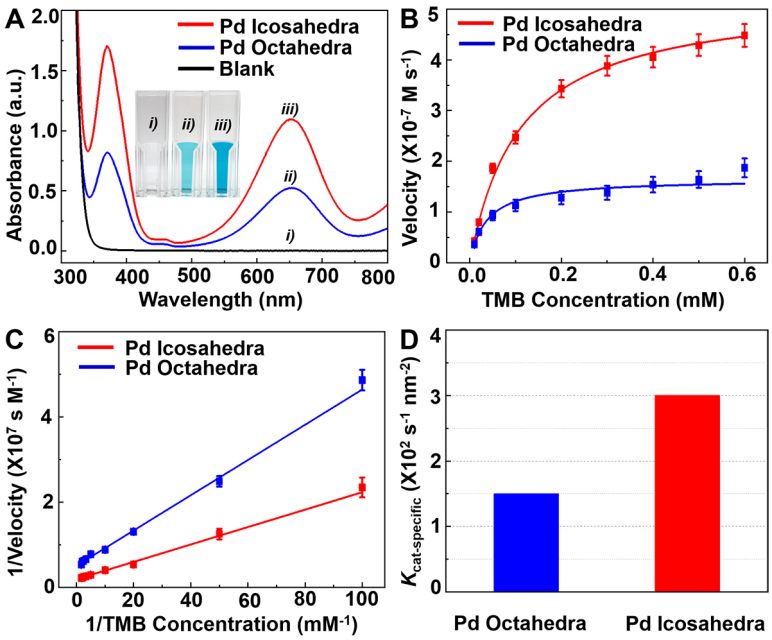

Figure 2. (A) UV-vis spectra taken from reaction solutions (*i.e.*, oxidation of TMB by H_2O_2) catalyzed by Pd octahedra and icosahedra of the same particle concentration at t = 1 min. Inset is photographs of corresponding reaction solutions; (B, C) Kinetic assays of the catalytic reaction toward TMB. Error bars indicate standard deviations of three independent measurements; (D) A histogram comparing the $K_{\text{cat-specific}}$ values of Pd octahedra and icosahedra.

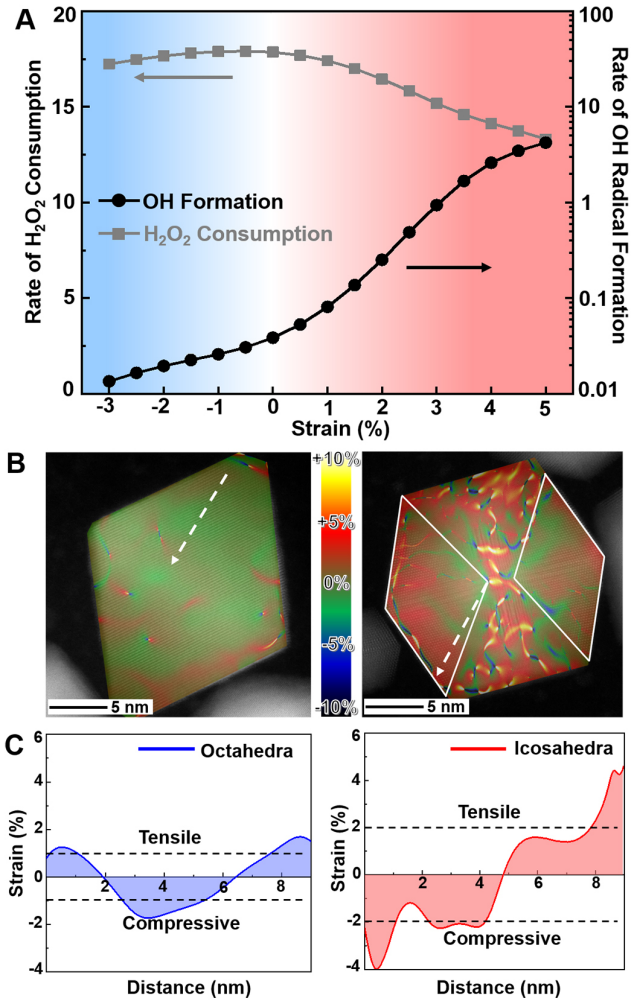

Figure 3. (A) Predicted rates of H_2O_2 consumption and OH radical formation (in s^{-1}·$site^{-1}$) on Pd (111) as a function of surface strain from a microkinetic model based on self-consistent GGA-RPBE energies; see SI for parameters and simulated conditions. (B) Surface strain mapping for Pd octahedron and icosahedron through GPA. Note, signal from regions outside the areas marked by two white quadrilaterals is the noise caused by blurring STEM image.[42] (C) Strain distribution along the white arrows in (B) for Pd octahedron and icosahedron.

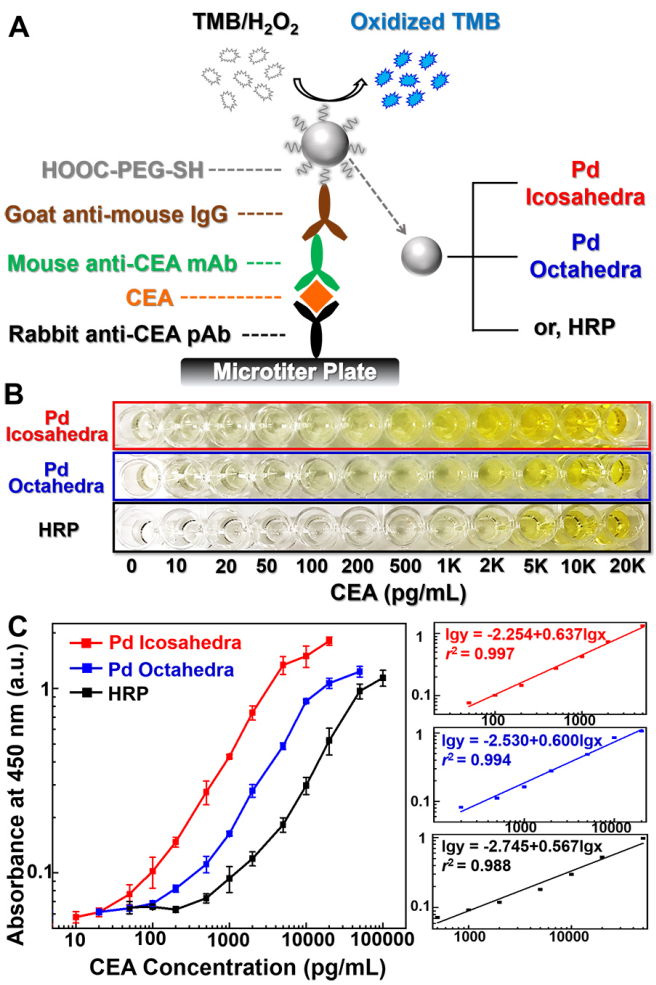

Figure 4. (A) Schematics of the colorimetric ELISAs of CEA; (B) Photographs taken from the detection of CEA standards with the Pd icosahedra-ELISA (top), Pd octahedra-ELISA (middle), and HRP-ELISA (bottom); (C) Corresponding calibration curves (left) and the linear ranges (right) of the detection results shown in (B). Error bars indicate standard deviations of eight independent measurements.